

# A C<sub>1</sub> Microkinetic Model for Methane Conversion to Syngas on Rh/Al<sub>2</sub>O<sub>3</sub>

**Matteo Maestri**

Dept. of Chemical Engineering and Center for Catalytic Science and Technology (CCST), University of Delaware, Newark, DE, 19716, and Laboratory of Catalysis and Catalytic Processes, Dipartimento di Energia, Politecnico di Milano, Piazza Leonardo da Vinci 32, 20133 Milan, Italy

**Dionisios G. Vlachos**

Dept. of Chemical Engineering and Center for Catalytic Science and Technology (CCST), University of Delaware, Newark, DE, 19716

**Alessandra Beretta, Gianpiero Groppi, and Enrico Tronconi**

Laboratory of Catalysis and Catalytic Processes, Dipartimento di Energia, Politecnico di Milano, Piazza Leonardo da Vinci 32, 20133 Milan, Italy

DOI 10.1002/aic.11767

Published online February 20, 2009 in Wiley InterScience (www.interscience.wiley.com).

*A microkinetic model capable of describing multiple processes related to the conversion of natural gas to syngas and hydrogen on Rh is derived. The parameters of microkinetic models are subject to (intrinsic) uncertainty arising from estimation. It is shown that intrinsic uncertainty could markedly affect even qualitative model predictions (e.g., the rate-determining step). In order to render kinetic models predictive, we propose a hierarchical, data-driven methodology, where microkinetic model analysis is combined with a comprehensive, kinetically relevant set of nearly isothermal experimental data. The new, thermodynamically consistent model is capable of predicting several processes, including methane steam and dry reforming, catalytic partial oxidation, H<sub>2</sub> and CO rich combustion, water-gas shift and its reverse at different temperatures, space velocities, compositions and reactant dilutions, using the measured Rh dispersion as an input. Comparison with other microkinetic models is undertaken. Finally, an uncertainty analysis assesses the effect of intrinsic uncertainty and catalyst heterogeneity on the overall model predictions. © 2009 American Institute of Chemical Engineers AIChE J, 55: 993–1008, 2009*

**Keywords:** microkinetic modeling, catalytic partial oxidation, steam reforming, dry reforming, water-gas shift, catalytic combustion, uncertainty analysis, parameter refinement, methane, Rh

## Introduction

Global climate changes and the need to reduce greenhouse gas emissions have stimulated a growing interest in alternative, clean fuels. Natural gas and hydrogen are two such fuels. The former is naturally abundant and is usually con-

verted to syngas. Aside from traditional uses of syngas in chemical industry (e.g., methanol and ammonia production), many new applications emerge. In power generation, the concept of syngas-enriched fuel in gas turbines is being exploited because highly reactive species, such as H<sub>2</sub> and CO, improve flame stability, allowing lower combustion temperatures and consequently considerable reduction of NO<sub>x</sub> emissions.<sup>1</sup> H<sub>2</sub>-assisted combustion has also been proposed for the conventional ICE (internal combustion engine), and onboard reforming could improve the performance of cata-

Correspondence concerning this article should be addressed to D. G. Vlachos at vlachos@udel.edu.

**Table 1. Experimental Data Sets**

Tag	Flow-rate (mol/min)	CH <sub>4</sub> , %	O <sub>2</sub> , %	CO, %	CO <sub>2</sub> , %	H <sub>2</sub> , %	H <sub>2</sub> O, %	Temperature range [°C]	Comments
SR1	0.01670	1.04	0.72	0.00	0.00	1.49	0.00	300–850	
SR2	0.01724	1.03	0.96	0.00	0.00	1.98	0.00	300–850	
SR3	0.01707	1.05	1.30	0.00	0.00	2.54	0.00	300–850	Assessment
DR4	0.01338	1.04	0.00	0.00	1.01	0.00	0.00	300–850	Assessment
DR5	0.01327	1.00	0.00	0.00	2.02	0.00	0.00	300–850	
DR6	0.01371	1.06	0.00	0.00	3.85	0.00	0.00	300–850	Assessment
DR7	0.01347	2.09	0.00	0.00	3.92	0.00	0.00	300–850	Assessment
WGS	0.01274	0.00	0.00	1.59	0.00	0.00	2.39	300–550	
RWGS 1	0.01321	0.00	0.00	0.00	1.09	1.02	0.00	300–850	Assessment
RWGS 2	0.01321	0.00	0.00	0.00	1.00	2.00	0.00	300–850	
H2 1	0.01579	0.00	0.51	0.00	0.00	2.05	0.00	25–300	
H2 2	0.03486	0.00	0.51	0.00	0.00	4.13	0.00	25–300	
H2 4	0.03443	0.00	0.51	0.00	0.00	4.13	0.00	25–300	Assessment
H2 5	0.03120	0.00	0.52	0.00	0.00	2.08	0.00	25–300	Assessment
CO 1	0.03126	0.79	0.00	2.02	0.00	0.00	0.00	25–300	
CO 3	0.00824	0.00	0.42	1.06	0.00	0.00	0.00	25–300	
CO 4	0.01549	0.00	0.42	1.05	0.00	0.00	0.00	25–300	Assessment
CPO1	0.01550	1.04	1.03	0.00	0.00	0.00	0.00	300–850	
CPO2	0.03494	1.03	0.58	0.00	0.00	0.00	0.00	300–850	
CPO3	0.00637	1.00	0.56	0.00	0.00	0.00	0.00	300–850	
CPO4	0.01723	1.05	0.56	0.00	1.08	0.00	0.02	300–850	Assessment
CPO5	0.01346	16.28	9.25	0.00	0.00	0.00	0.00	300–850	Assessment
CPO6	0.01452	27.27	15.31	0.00	0.00	0.00	0.00	300–850	Assessment
CPO7	0.01358	8.51	4.78	0.00	0.00	0.00	0.00	300–850	Assessment
CPO9	0.01358	1.02	0.57	0.00	0.00	0.00	0.00	300–850	Assessment
CPO10	0.01305	1.02	1.30	0.00	0.00	0.00	0.00	300–850	Assessment

Annular Reactor – I.D. 4 mm – O.D. 5 mm – length 22 mm – Balance N<sub>2</sub>.

lytic mufflers,<sup>2–4</sup> as well as the regeneration of lean-NO<sub>x</sub> traps.<sup>5,6</sup> Utilization of remote and offshore natural gas reserves for liquid products<sup>7</sup> (gas-to-liquid, GTL) further stimulates research involving syngas. For a hydrogen-based fuel economy, hydrogen should be easily available and affordable. The centralized hydrogen production and delivery would require a significant capital investment for infrastructure,<sup>8,9</sup> and hydrogen storage does not appear as a short-term solution. An alternative approach could entail the direct production of H<sub>2</sub> onboard or in stationary applications, starting from fuels that are easier to deliver and/or store, such as natural gas.<sup>8</sup>

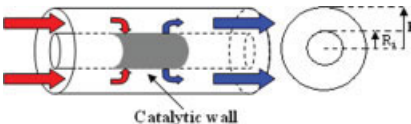
These novel applications of syngas require small scale, decentralized (both stationary and onboard) reforming of hydrocarbons with severe constraints on reactor size and fast responses to transients. Consequently, syngas production at the micro- and mesoscales is receiving increased attention, whereby the traditional steam reforming on Ni is replaced with a process running in small reactors.<sup>10,11</sup>

Catalytic partial oxidation (CPO) on noble metals is a promising process alternative to the traditional steam reforming. Studied since the 1940s for syngas production, this technology has become popular in the last 15 years, after Schmidt and coworkers reported excellent conversions and selectivities to syngas in short contact time reactors, using Pt or Rh as catalysts.<sup>12–14</sup> Millisecond, autothermal operation ensures compact reactors.<sup>15</sup> Moreover, noble metals are very good catalysts also for other processes that may play an important role in a H<sub>2</sub>-driven economy, such as CH<sub>4</sub> steam reforming (SR), CH<sub>4</sub> dry reforming (DR), and water-gas shift (WGS).<sup>16</sup>

The design and scaleup of these processes require reliable kinetic models, which are valid over a wide range of operating conditions. Microkinetic models represent the most

promising and reliable tool.<sup>17</sup> Differently from the classical approach used in catalysis, microkinetic modeling does not require *a priori* assumptions about the rate determining step (RDS) or the most abundant reactive intermediate (MARI), and, in principle, can capture the reacting system behavior under significantly different operating conditions. Moreover, it can be used for identification of the dominant elementary paths on the catalyst surface, and as an important tool for the consolidation of fundamental information under different operating conditions.<sup>17–20</sup>

**Table 2. Governing Equations and Reactor Parameters**

Model Equations
$\frac{dW_i}{dV} = k_{mat,i} \rho_{av} (\omega_i^{wall} - \omega_i^{bulk}) \quad (1)$
$k_{mat,i} \rho_{av} (\omega_i^{wall} - \omega_i^{bulk}) = \left( \sum_{j=1}^{NR} v_{i,j} r_j \right) a_{Rh} MW_i \quad (2)$
$Sh_i = \frac{k_{mat,i} d_h}{D_i} = 5.21 + 6.874 \cdot \exp(-71.2 \cdot z_i^*) \cdot (1000 \cdot z_i^*)^{-0.35} \quad (3)$
<p>where: <math>z_i^* = \frac{D_i z}{v d_h^2}</math> (Ref. 34)</p>
Reactor Configuration and Parameters
 <p>Annular Reactor Inner Radius (R<sub>i</sub>): 0.2 cm Outer Radius (R<sub>o</sub>): 0.25 cm Reactor Length: 2.2 cm</p>

[Color figure can be viewed in the online issue, which is available at [www.interscience.wiley.com](http://www.interscience.wiley.com).]

In this work, we propose a hierarchical data-driven methodology for the refinement of microkinetic model parameters, where sensitivity analysis (SA) and microkinetic modeling are used symbiotically to refine model parameters and derive predictive microkinetic models. To this end, we employ a comprehensive set of nearly-isothermal experimental data<sup>21,22</sup> to improve the C<sub>1</sub> microkinetic model of Mhadeshwar and Vlachos.<sup>23</sup> Extensive assessment of the new model is performed, and a comparison with other microkinetic models is undertaken. Finally, an uncertainty analysis with respect to key parameters of the model is presented.

### Original mechanism analysis and refinement

The construction of a microkinetic model involves setting-up a comprehensive sequence of elementary reactions and the estimation of rate parameters. Estimation of rate parameters (including coverage dependencies in activation energies) subject to thermodynamic consistency is a challenge, especially for large reaction networks. In this respect, Vlachos and coworkers have proposed a hierarchical multiscale methodology for the development of predictive surface reaction mechanisms.<sup>23–27</sup> The approach encompasses semiempirical methods (e.g., the Unity Bond Index—Quadratic Exponential Potential, UBI-QEP, framework<sup>28</sup>), and first-principle techniques, such as density functional theory (DFT). Nevertheless, the model parameters, even if physically sound, are subject to the intrinsic uncertainty of the calculation methods (e.g., binding and activation energies computed with DFT have an accuracy of the order of 5 kcal/mol<sup>29,30</sup>), and the heterogeneity of real catalysts (e.g., presence of defects on the surface can considerably affect activation energies and makes first-principle-based predictions of reaction parameters for surface reactions a challenging task<sup>31</sup>).

In order to make a microkinetic model quantitatively predictive and reliable, the parameters must be fine-tuned, using kinetically relevant experimental data, within the uncertainty range. However, due to the very large number of parameters usually incorporated in microkinetic models, a simple optimization could give models that are either valid over a limited range of operating conditions or incapable of being quantitatively predictive.

Here, based on analysis of a comprehensive set of experimental data, we show how parameter uncertainty can markedly affect model predictions, and we propose a hierarchical, data-driven refinement methodology for tuning model parameters within the uncertainty range.

### Experimental data sets

The experimental tests were performed in an annular reactor at short-contact times. The reactor consisted of a catalyst-coated alumina tube coaxially inserted into a quartz-tube. Inside the alumina tube, a sliding thermocouple was inserted, in order to measure catalyst temperature profiles.<sup>32,33</sup> The catalyst weight was of the order of 10 mg (4% Rh/ $\alpha$ -Al<sub>2</sub>O<sub>3</sub>), and the Rh dispersion for the aged-catalyst was estimated, from CO and H<sub>2</sub> chemisorption experiments, to be 5%. For this rig, this corresponds to a Rh specific surface of 600 cm<sup>2</sup>/cm<sup>3</sup>.

The kinetic study consists of a comprehensive data set, including CPO, H<sub>2</sub>O and CO<sub>2</sub> reforming, WGS, reverse-

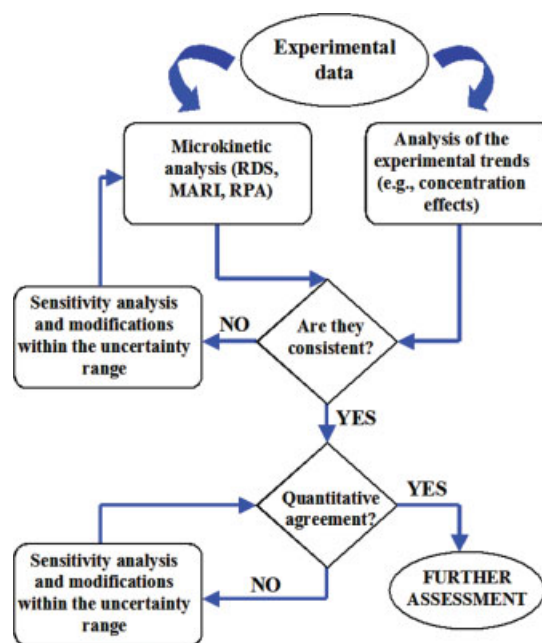


**Figure 1. Schematic of the hierarchical, data-driven refinement methodology.**

[Color figure can be viewed in the online issue, which is available at [www.interscience.wiley.com](http://www.interscience.wiley.com).]

WGS, H<sub>2</sub>, and CO rich combustion.<sup>21,22</sup> All the experiments were performed at atmospheric pressure from 300 to 850 °C (increments of 10–50 °C), with a gas hourly space velocity (GHSV) varying from  $8 \times 10^5$  to  $4.5 \times 10^6$  NL/kg<sub>cat</sub>/h, in diluted conditions (N<sub>2</sub> > 95%) under nearly isothermal conditions. In addition, CPO tests of concentrated mixtures were also carried out. A summary of all the experimental tests considered in this work is reported in Table 1: experiments were conducted for seven processes, at multiple compositions, giving rise to 26 sets. For each set, several temperatures were studied, giving rise to more than 300 experimental points. Experiments labeled as “assessment” were conducted after the model was developed, and were considered only for model assessment rather than for model refinement.

### Original kinetic model

The mechanism of Mhadeshwar and Vlachos<sup>23</sup> consists of 104 elementary reactions and was developed to describe among others methane CPO and reforming, WGS, and oxygenate (methanol and formaldehyde) decomposition on Rh. Activation energies were calculated with the UBI-QEP framework.<sup>28</sup> Adsorbate-adsorbate interactions in heats of chemisorption are considered for O\*, H\*, H<sub>2</sub>O\*, CO\* and OH\*-O\*, H<sub>2</sub>O\*-OH, CO\*-H\*, on the basis either of experimental data or DFT calculations. The model is thermodynamically consistent at both the entropic and enthalpic level.<sup>25</sup>

### Original model results and need for parameter refinement

We simulated the experimental data of Donazzi et al.<sup>21</sup> using a 1D heterogeneous mathematical model. External mass-transfer limitations have been accounted for using a specific correlation for the annular reactor,<sup>34</sup> while the exper-

Table 3. Surface Reaction Mechanism

No.	Reaction	A (unitless or s <sup>-1</sup> )	beta	Bond index	Activation Energy [kcal/mol] and {typical estimations for $\theta_O = 0.9$ and for $\theta_H = 0.1$ and $\theta_{CO} = 0.05$ at 1173.15K}
1	H <sub>2</sub> + 2* → 2H*	7.73 × 10 <sup>-01</sup>	0.9387	0.5	0.0
2	2H* → H <sub>2</sub> + 2*	5.56 × 10 <sup>+11</sup>	-0.4347	0.5	20.4 - 5 $\theta_H$ - 7.4 $\theta_{CO}$ + f(T) {12.7; 11.7}
3	O <sub>2</sub> + 2* → 2O*	4.81 × 10 <sup>-02</sup>	1.9965	0.5	0.0
4	2O* → O <sub>2</sub> + 2*	4.31 × 10 <sup>+12</sup>	1.1995	0.5	80.9 - 52.0 $\theta_O$ + f(T) {27.0; 73.8}
5	OH* + * → H* + O*	5.20 × 10 <sup>+12</sup>	-0.2659	0.3	14.5 + f( $\theta_O, \theta_H, \theta_{CO}, \theta_{H_2O}, T$ ) {12.3; 15.4}
6	H* + O* → OH* + *	4.69 × 10 <sup>+12</sup>	-0.8196	0.3	4.6 + f( $\theta_O, \theta_H, \theta_{CO}, \theta_{H_2O}, T$ ) {4.4; 0.48}
7	H <sub>2</sub> O* + * → H* + OH*	5.74 × 10 <sup>+11</sup>	0.0281	0.55	16.9 + f( $\theta_O, \theta_{OH}, \theta_H, \theta_{CO}, \theta_{H_2O}, T$ ) {31.9; 18.7}
8	H* + OH* → H <sub>2</sub> O* + *	1.80 × 10 <sup>+09</sup>	1.2972	0.55	19.1 + f( $\theta_O, \theta_{OH}, \theta_H, \theta_{CO}, \theta_{H_2O}, T$ ) {0.0; 16.0}
9	H <sub>2</sub> O* + O* → 2OH*	2.08 × 10 <sup>+13</sup>	-2.1130	0.3	6.9 + f( $\theta_O, \theta_{OH}, \theta_{H_2O}, T$ ) {24.0; 6.4}
10	2OH* → H <sub>2</sub> O* + O*	7.22 × 10 <sup>+10</sup>	-0.2902	0.3	19.0 + f( $\theta_O, \theta_{OH}, \theta_{H_2O}, T$ ) {19.0; 18.3}
11	OH + * → OH*	2.66 × 10 <sup>-01</sup>	-0.2891	0.5	0.0
12	OH* → OH + *	1.14 × 10 <sup>+13</sup>	-0.9500	0.5	70.0 - 33.0 $\theta_O$ - 25.0 $\theta_{H_2O}$ + f(T) {36.8; 66.5}
13	H <sub>2</sub> O + * → H <sub>2</sub> O*	7.72 × 10 <sup>-02</sup>	1.4067	0.5	0.0
14	H <sub>2</sub> O* → H <sub>2</sub> O + *	2.06 × 10 <sup>+13</sup>	-1.8613	0.5	10.8 - 25.0 $\theta_{OH}$ - 4.5 $\theta_{H_2O}$ + f(T) {6.5; 6.5}
15	H + * → H*	1.93 × 10 <sup>-01</sup>	1.5313	0.5	0.0
16	H* → H + *	2.40 × 10 <sup>+12</sup>	1.3208	0.5	62.3 - 2.5 $\theta_H$ - 3.7 $\theta_{CO}$ + f(T) {59.7; 59.2}
17	O + * → O*	4.46 × 10 <sup>-02</sup>	-1.9236	0.5	0.0
18	O* → O + *	9.74 × 10 <sup>+12</sup>	-1.9701	0.5	100.0 - 26.0 $\theta_O$ + f(T) {74.0; 97.4}
19	CO + * → CO*	5.00 × 10 <sup>-01</sup>	-2.0000	0.5	0.0
20	CO* → CO + *	5.65 × 10 <sup>+12</sup>	1.9879	0.5	38.5 - 3.7 $\theta_H$ - 15.0 $\theta_{CO}$ + f(T) {35.0; 34.3}
21	CO <sub>2</sub> + * → CO <sub>2</sub> *	3.67 × 10 <sup>-01</sup>	-2.3294	0.5	0.0
22	CO <sub>2</sub> * → CO <sub>2</sub> + *	7.54 × 10 <sup>+10</sup>	2.1831	0.5	5.2 + f(T) {1.7; 1.7}
23	CO <sub>2</sub> * + * → CO* + O*	4.12 × 10 <sup>+09</sup>	1.9698	0.9	19.5 + f( $\theta_O, \theta_H, \theta_{CO}, T$ ) {40.0; 21.0}
24	CO* + O* → CO <sub>2</sub> * + *	3.27 × 10 <sup>+09</sup>	1.3560	0.9	25.6 + f( $\theta_O, \theta_H, \theta_{CO}, T$ ) {19.3; 23.0}
25	COOH + * → COOH*	5.34 × 10 <sup>-01</sup>	-1.0767	0.5	0.0
26	COOH* → COOH + *	1.12 × 10 <sup>+11</sup>	1.6803	0.5	62.2 + f(T) {57.9; 57.9}
27	HCOO + 2* → HCOO**	1.89 × 10 <sup>-02</sup>	-0.5548	0.5	0.0
28	HCOO** → HCOO + 2*	3.74 × 10 <sup>+13</sup>	0.5548	0.5	69.2 + f(T) {64.9; 64.9}
29	CO <sub>2</sub> * + H* → CO* + OH*	7.99 × 10 <sup>+13</sup>	0.0301	0.7	6.1 + f( $\theta_O, \theta_H, \theta_{CO}, \theta_{H_2O}, T$ ) {21.5; 4.1}
30	CO* + OH* → CO <sub>2</sub> * + H*	7.02 × 10 <sup>+13</sup>	-0.0301	0.7	22.2 + f( $\theta_O, \theta_H, \theta_{CO}, \theta_{H_2O}, T$ ) {8.7; 20.9}
31	COOH* + * → CO* + OH*	1.07 × 10 <sup>+12</sup>	-0.4123	0.5	6.2 + f( $\theta_O, \theta_H, \theta_{CO}, \theta_{H_2O}, T$ ) {20.0; 6.8}
32	CO* + OH* → COOH* + *	9.37 × 10 <sup>+11</sup>	0.4123	0.5	18.6 + f( $\theta_O, \theta_H, \theta_{CO}, \theta_{H_2O}, T$ ) {0.0; 15.8}
33	COOH* + * → CO <sub>2</sub> * + H*	1.00 × 10 <sup>+10</sup>	-0.4424	0.5	4.23 + f( $\theta_H, \theta_{CO}, T$ ) {7.3; 7.8}
34	CO <sub>2</sub> * + H* → COOH* + *	9.99 × 10 <sup>+09</sup>	0.4424	0.5	0.6 + f( $\theta_H, \theta_{CO}, T$ ) {0.0; 0.0}
35	CO* + H <sub>2</sub> O* → COOH* + H*	3.34 × 10 <sup>+11</sup>	-0.2222	0.5	20.7 + f( $\theta_{OH}, \theta_H, \theta_{CO}, \theta_{H_2O}, T$ ) {20.6; 20.5}
36	COOH* + H* → CO* + H <sub>2</sub> O*	1.20 × 10 <sup>+09</sup>	0.2223	0.5	10.5 + f( $\theta_{OH}, \theta_H, \theta_{CO}, \theta_{H_2O}, T$ ) {8.7; 8.8}
37	CO <sub>2</sub> * + OH* → COOH* + O*	1.05 × 10 <sup>+11</sup>	0.7192	0.5	22.3 + f( $\theta_O, \theta_{H_2O}, T$ ) {16.5; 21.6}
38	COOH* + O* → CO <sub>2</sub> * + OH*	9.51 × 10 <sup>+10</sup>	-0.7192	0.5	16.0 + f( $\theta_O, \theta_{H_2O}, T$ ) {15.9; 16.0}
39	CO <sub>2</sub> * + H <sub>2</sub> O* → COOH* + OH*	1.78 × 10 <sup>+12</sup>	-0.1922	0.5	13.5 + f( $\theta_O, \theta_{OH}, \theta_{H_2O}, T$ ) {24.6; 12.9}
40	COOH* + OH* → CO <sub>2</sub> * + H <sub>2</sub> O*	5.60 × 10 <sup>+09</sup>	0.1922	0.5	19.4 + f( $\theta_O, \theta_{OH}, \theta_{H_2O}, T$ ) {0.0; 18.0}
41	CO <sub>2</sub> * + H* → HCOO**	1.04 × 10 <sup>+09</sup>	1.1254	0.5	4.2 + f( $\theta_H, \theta_{CO}, T$ ) {0.2; 4.2}
42	HCOO** → CO <sub>2</sub> * + H*	3.86 × 10 <sup>+13</sup>	-1.1253	0.5	0.0 + f( $\theta_H, \theta_{CO}, T$ ) {0.0; 0.3}
43	CO <sub>2</sub> * + OH* + * → HCOO** + O*	1.09 × 10 <sup>+09</sup>	1.4022	0.5	27.6 + f( $\theta_O, \theta_{H_2O}, T$ ) {21.3; 26.7}
44	HCOO** + O* → CO <sub>2</sub> * + OH* + *	3.67 × 10 <sup>+13</sup>	-1.4022	0.5	13.4 + f( $\theta_O, \theta_{H_2O}, T$ ) {13.2; 12.3}
45	CO <sub>2</sub> * + H <sub>2</sub> O* + * → HCOO** + OH*	9.24 × 10 <sup>+09</sup>	0.4908	0.5	18.4 + f( $\theta_O, \theta_{OH}, \theta_{H_2O}, T$ ) {32.1; 17.6}
46	HCOO** + OH* → CO <sub>2</sub> * + H <sub>2</sub> O* + *	1.08 × 10 <sup>+12</sup>	-0.4908	0.5	16.4 + f( $\theta_O, \theta_{OH}, \theta_{H_2O}, T$ ) {0.0; 16.4}
47	C + * → C*	4.98 × 10 <sup>-02</sup>	-1.8618	0.5	0.0
48	C* → C + *	1.42 × 10 <sup>+13</sup>	1.8618	0.5	159.0 + f(T) {156.4; 156.4}
49	CH + * → CH*	2.29 × 10 <sup>-02</sup>	-1.0798	0.5	0.0
50	CH* → CH + *	3.08 × 10 <sup>+13</sup>	1.0798	0.5	151.2 + f(T) {147.7; 147.7}
51	CH <sub>2</sub> + * → CH <sub>2</sub> *	4.09 × 10 <sup>-02</sup>	-0.4265	0.5	0.0
52	CH <sub>2</sub> * → CH <sub>2</sub> + *	1.73 × 10 <sup>+13</sup>	0.4265	0.5	109.3 + f(T) {105.0; 105.0}
53	CH <sub>3</sub> + * → CH <sub>3</sub> *	1.35 × 10 <sup>-01</sup>	0.0326	0.5	0.0
54	CH <sub>3</sub> * → CH <sub>3</sub> + *	5.22 × 10 <sup>+12</sup>	-0.0325	0.5	42.4 + f(T) {38.1; 38.1}
55	CH <sub>4</sub> + 2* → CH <sub>3</sub> * + H*	5.72 × 10 <sup>-01</sup>	0.7883	0.5	9.8 + f( $\theta_H, \theta_{CO}, T$ ) {15.3; 15.6}
56	CH <sub>3</sub> * + H* → CH <sub>4</sub> + 2*	7.72 × 10 <sup>+10</sup>	-0.7883	0.5	9.5 + f( $\theta_H, \theta_{CO}, T$ ) {5.4; 5.1}
57	CH <sub>3</sub> * + * → CH <sub>2</sub> * + H*	2.49 × 10 <sup>+10</sup>	0.0862	0.5	10.6 + f( $\theta_H, \theta_{CO}, T$ ) {12.2; 12.3}
58	CH <sub>2</sub> * + H* → CH <sub>3</sub> * + *	2.57 × 10 <sup>+09</sup>	-0.0862	0.5	29.1 + f( $\theta_H, \theta_{CO}, T$ ) {25.9; 25.5}
59	CH <sub>2</sub> * + * → CH* + H*	5.50 × 10 <sup>+10</sup>	-0.1312	0.5	20.5 + f( $\theta_H, \theta_{CO}, T$ ) {21.7; 21.8}
60	CH* + H* → CH <sub>2</sub> * + *	7.27 × 10 <sup>+09</sup>	0.1312	0.5	23.6 + f( $\theta_H, \theta_{CO}, T$ ) {20.9; 20.5}
61	CH* + * → C* + H*	4.58 × 10 <sup>+12</sup>	-0.2464	0.5	27.6 + f( $\theta_H, \theta_{CO}, T$ ) {28.9; 29.0}
62	C* + H* → CH* + *	2.18 × 10 <sup>+11</sup>	0.2464	0.5	17.1 + f( $\theta_H, \theta_{CO}, T$ ) {14.3; 14.0}
63	CH <sub>3</sub> * + O* → CH <sub>2</sub> * + OH*	2.96 × 10 <sup>+11</sup>	-0.1906	0.5	7.1 + f( $\theta_O, \theta_{H_2O}, T$ ) {2.9; 6.4}
64	CH <sub>2</sub> * + OH* → CH <sub>3</sub> * + O*	3.38 × 10 <sup>+10</sup>	0.1906	0.5	35.5 + f( $\theta_O, \theta_{H_2O}, T$ ) {24.4; 34.3}
65	CH* + OH* → CH <sub>2</sub> * + O*	3.83 × 10 <sup>+10</sup>	0.4081	0.5	32.6 + f( $\theta_O, \theta_{H_2O}, T$ ) {25.2; 31.9}
66	CH <sub>2</sub> * + O* → CH* + OH*	2.61 × 10 <sup>+11</sup>	-0.4081	0.5	19.6 + f( $\theta_O, \theta_{H_2O}, T$ ) {18.2; 18.6}
67	C* + OH* → CH* + O*	2.30 × 10 <sup>+10</sup>	0.5232	0.5	29.8 + f( $\theta_O, \theta_{H_2O}, T$ ) {21.3; 29.2}



Table 3. (Continued)

No.	Reaction	A (unitless or s <sup>-1</sup> )	beta	Bond index	Activation Energy [kcal/mol] and {typical estimations for $\theta_O = 0.9$ and for $\theta_H = 0.1$ and $\theta_{CO} = 0.05$ at 1173.15K}
68	CH* + O* → C* + OH*	$4.35 \times 10^{+11}$	-0.5232	0.5	$30.4 + f(\theta_O, \theta_{H_2O}, T)$ {28.0; 29.5}
69	CH <sub>2</sub> * + H <sub>2</sub> O* → CH <sub>3</sub> * + OH*	$5.73 \times 10^{+10}$	-0.7208	0.5	$21.3 + f(\theta_O, \theta_{OH}, \theta_{H_2O}, T)$ {45.6; 20.0}
70	CH <sub>3</sub> * + OH* → CH <sub>2</sub> * + H <sub>2</sub> O*	$1.74 \times 10^{+09}$	0.7208	0.5	$5.1 + f(\theta_O, \theta_{OH}, \theta_{H_2O}, T)$ {0.0; 4.2}
71	CH* + H <sub>2</sub> O* → CH <sub>2</sub> * + OH*	$6.49 \times 10^{+11}$	-0.5033	0.5	$21.8 + f(\theta_O, \theta_{OH}, \theta_{H_2O}, T)$ {31.1; 21.1}
72	CH <sub>2</sub> * + OH* → CH* + H <sub>2</sub> O*	$1.54 \times 10^{+10}$	0.5033	0.5	$20.9 + f(\theta_O, \theta_{OH}, \theta_{H_2O}, T)$ {0.0; 19.7}
73	C* + H <sub>2</sub> O* → CH* + OH*	$9.74 \times 10^{+11}$	-0.3882	0.5	$17.6 + f(\theta_O, \theta_{OH}, \theta_{H_2O}, T)$ {23.4; 16.8}
74	CH* + OH* → C* + H <sub>2</sub> O*	$6.41 \times 10^{+10}$	0.3882	0.5	$30.3 + f(\theta_O, \theta_{OH}, \theta_{H_2O}, T)$ {6.1; 30.3}
75	CO* + * → C* + O*	$1.25 \times 10^{+09}$	0.5712	0.5	$49.1 + f(\theta_O, \theta_H, \theta_{CO}, T)$ {64.1; 49.1}
76	C* + O* → CO* + *	$7.22 \times 10^{+09}$	-0.5712	0.5	$12.3 + f(\theta_O, \theta_H, \theta_{CO}, T)$ {0.0; 10.0}
77	CO* + H* → CH* + O*	$9.07 \times 10^{+09}$	0.8176	0.8	$69.1 + f(\theta_O, \theta_H, \theta_{CO}, T)$ {79.1; 66.9}
78	CH* + O* → CO* + H*	$1.10 \times 10^{+12}$	-0.8176	0.8	$42.9 + f(\theta_O, \theta_H, \theta_{CO}, T)$ {29.5; 42.0}
79	CO* + H* → C* + OH*	$1.18 \times 10^{+12}$	0.2944	0.15	$26.8 + f(\theta_O, \theta_H, \theta_{CO}, \theta_{H_2O}, T)$ {56.2; 25.3}
80	C* + OH* → CO* + H*	$7.60 \times 10^{+12}$	-0.2944	0.15	$0.0 + f(\theta_O, \theta_H, \theta_{CO}, \theta_{H_2O}, T)$ {0.0; 0.0}
81	2CO* → C* + CO <sub>2</sub> *	$1.11 \times 10^{+09}$	0.2644	0.5	$42.9 + f(\theta_H, \theta_{CO}, T)$ {43.5; 41.2}
82	C* + CO <sub>2</sub> * → 2CO*	$8.10 \times 10^{+09}$	-0.2644	0.5	$0.0 + f(\theta_H, \theta_{CO}, T)$ {0.0; 0.0}

The mechanism will be available to download from [www.dion.che.udel.edu](http://www.dion.che.udel.edu) or by requesting it from the authors.  
The reaction rate constant ( $k$ ) is calculated as follows:

$$k = \frac{A}{\Gamma_{Rh}^{n-1}} \left( \frac{T}{T_0} \right)^\beta e^{-E/RT} \quad \text{or} \quad k = \frac{s}{\Gamma_{Rh}^n} \sqrt{\frac{RT}{2\pi MW}} \left( \frac{T}{T_0} \right)^\beta e^{-E/RT},$$

where  $A$  is the pre-exponential,  $s$  is the sticking coefficient,  $\Gamma_{Rh}$  is the site density,  $n$  is the reaction order,  $E$  is the activation energy,  $R$  is the ideal gas constant and  $T_0$  is the reference temperature (300 K). Activation energies are calculated according to the UBI-QEP framework<sup>28</sup> and the expressions are given in Table 6. In the simulations,  $\Gamma_{Rh}$  has been set equal to  $2.49 \times 10^{-9}$  mol/cm<sup>2</sup>. The  $i$ -th reaction rate is calculated according to:

$$r_i = k_i \prod_{j=1}^{K_{tot}} X_j^{v_{i,j}} = k_i \Gamma_{Rh}^n \prod_{j=1}^{K_{surf}} \theta_j^{v_{i,j}} \quad \text{for surface reaction}$$

or

$$r_i = k_i \prod_{j=1}^{K_{tot}} X_j^{v_{i,j}} = k_i \Gamma_{Rh}^n X_{\text{gas species}}^{v_i} \prod_{j=1}^{K_{surf}} \theta_j^{v_{i,j}} \quad \text{for adsorption reaction.}$$

Here  $X_j$  is the mole concentration either of gas species (mol/cm<sup>3</sup>) or adspecies (mol/cm<sup>2</sup>);  $\theta_j$  is the site fraction;  $r_i$  is the rate of the  $i$ th reaction (mol/cm<sup>2</sup>/s).

imental temperature profile has been input in each simulation. When the temperature varies significantly with position (nondilute mixtures), for convenience in the graphs the results are plotted vs. the average reactor temperature. Model equations and details about the annular reactor are reported in Table 2.

Simulations pointed out deviations between the original model predictions and experimental data. In particular, different values of Rh surface area per unit reactor volume were needed to correctly reproduce the conversion vs. temperature data. These specific surfaces ranged from 20 cm<sup>2</sup>/cm<sup>3</sup> for CO-rich experiments, to 20,000 cm<sup>2</sup>/cm<sup>3</sup> for CPO tests. Since all the experiments were performed on the same catalyst sample, such a huge difference in Rh specific surface was unacceptable. Moreover, quantitative agreement was not always satisfactory and some important features inferred from experiments, such as the reaction orders with respect to the reactants, were not always reproduced. A more detailed comparison of this model to all data is presented later. A need for parameter refinement was apparent.

One may naturally ask the question why microkinetic models are most often limited to describing a single process or a small dataset. First, it takes effort to develop a model capable of describing multiple processes. Second and more fundamental is the fact that there is a lack of kinetic relevant data for multiple processes with a well-characterized catalyst.

We are often confronted with “heterogeneous” data that come from different laboratories on different catalyst samples (different supports, preparation methods, precursors, and frequently noncharacterized or reported surface area) having variable (usually unknown) levels of measurement accuracy. This gives an undesirable flexibility to a modeler, but it has

Table 4. Heats of Chemisorption

Species	Heat of chemisorption [kcal/mol]	Temperature dependence (Q(T <sub>0</sub> )-Q(T))/R <sub>g</sub> ΔT
O*	100.0 - 26.0θ <sub>O</sub>	1.5
H*	62.3 - 3.7θ <sub>CO</sub> - 2.5θ <sub>H</sub>	1.5
OH*	70.0 - 33θ <sub>O</sub> + 25θ <sub>H<sub>2</sub>O</sub>	2
H <sub>2</sub> O*	10.8 + 25θ <sub>OH</sub> - 4.5θ <sub>H<sub>2</sub>O</sub>	2.5
CO*	38.5 - 15θ <sub>CO</sub> - 3.7θ <sub>H</sub>	2
CO <sub>2</sub> *	5.2	2
COOH*	62.2	2.5
HCOO**	69.2	2.5
C*	159.0	1.5
CH*	151.2	2
CH <sub>2</sub> *	109.3	2.5
CH <sub>3</sub> *	42.4	2.5
CH <sub>4</sub>	6.0	2.0

Temperature dependence of the heat of chemisorption has been taken into account via statistical mechanics.<sup>25</sup> For details see Ref. 23 and references therein.

**Table 5. Summary of Equations for Computing Activation Energies of Surface Reactions According to UBI-QEP Framework<sup>28</sup>**

Reaction type	Activation Energy	Notes
$AB + 2* \rightarrow A* + B*$ (dissociative adsorption)	$E_f = \phi \left[ \Delta H_{surf,f} - Q_{AB} + \frac{Q_A Q_B}{Q_A + Q_B} \right]$	$\Delta H_{surf,f} = D_{AB} - Q_A - Q_B$ $D_{AB} = H_A + H_B - H_{AB}$
$AB* + * \rightarrow A* + B*$ (dissociation reaction)	$E_f = \phi \left[ \Delta H_{surf,f} + \frac{Q_A Q_B}{Q_A + Q_B} \right]$	$\Delta H_{surf,f} = D_{AB} - Q_A - Q_B$ $D_{AB} = H_A + H_B - H_{AB}$
$A* + B* \rightarrow C* + D*$ (disproportionation reaction)	$E_f = \phi \left[ \Delta H_{surf,f} + \frac{Q_C Q_D}{Q_C + Q_D} \right]$	$\Delta H_{surf,f} = \Delta H_{gas,f} + Q_A + Q_B - Q_C - Q_D$ $D_{AB} = H_C + H_D - H_A - H_B$

For all reactions, the backward activation energy is  $E_b = E_f - \Delta H_{surf,f}$ . If either  $E_f$  or  $E_b$  becomes negative, it is set to zero and the other one equal to the heat of reaction. The dependence of heats of chemisorption on coverage and temperature is given in Table 4.  $H_i$  is the gas-phase enthalpy of the  $i$ th species,  $D$  is the gas-phase dissociation energy,  $\phi$  is the bond index ( $0 < \phi < 1$ ).

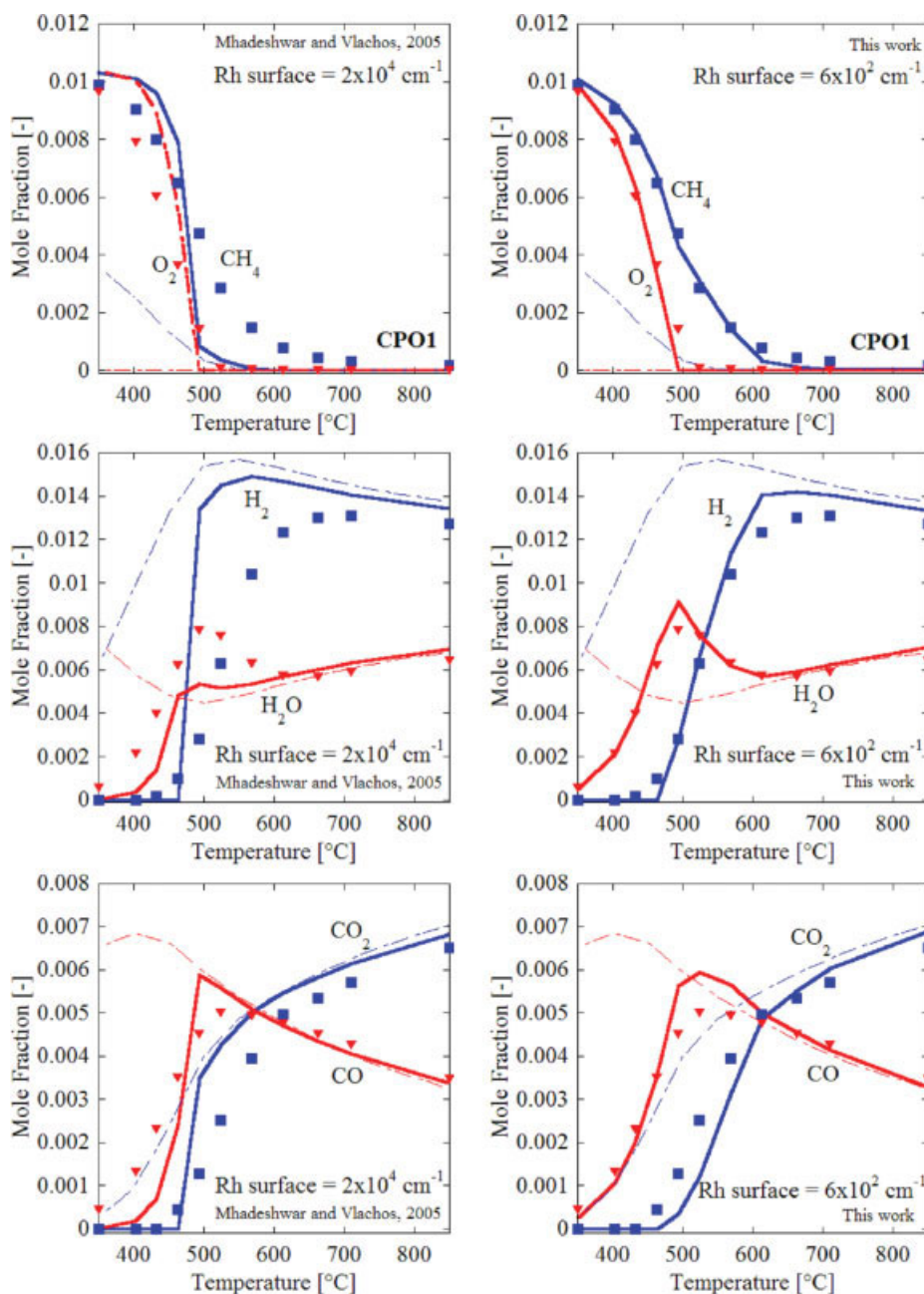


**Figure 2. Partial oxidation.**

Comparison between model prediction (solid lines) with the original model (left panels), and revised one (right panels), and experimental data (symbols) for CPO1 at different isothermal reactor temperatures. Conditions are reported in Table 1. Dash-dotted lines depict the equilibrium composition obtained using GasEq.<sup>45</sup> [Color figure can be viewed in the online issue, which is available at [www.interscience.wiley.com](http://www.interscience.wiley.com).]

until now been the method of choice when in need to consider comprehensive and diverse datasets, e.g., see the mechanism developed in Ref. 23. As shown in this article, this heterogeneous data approach has important (negative) ramifications for model development (see comparison of such models to data in the following).

### Hierarchical, data-driven refinement methodology

In order to refine the parameters, we employ the concept of data injection into the multiscale framework.<sup>27</sup> In particular, here we illustrate this general approach within the context of microkinetic modeling, using information extracted from microkinetic analysis of the experimental data. A schematic of the methodology is given in Figure 1. The approach entails qualitative (first pass) and quantitative (second pass) comparison of models to data and is iterative. Iterations terminate (convergence) when comparison to data is satisfactory. When convergence is not achieved, the elementary steps of the mechanism should be revisited. For each experiment, the RDS (obtained via SA), the MARI, and the main reaction paths were determined (a procedure often known as reaction path analysis (RPA)). In this way, we rationalize the effect of reactants and products on the overall reaction rate predicted by the model and compare with experimental findings. Reaction parameters were modified in order to obtain qualitative agreement with data. After qualitative agreement has been accomplished, SA with respect to pre-exponentials and activation energies of each reaction and heats of chemisorption of the species was performed in order to identify and refine important parameters within the range of their uncertainty. Specifically, pre-exponentials were modified within the range specified from transition state theory (TST),<sup>17</sup> and activation energies were modified by changing either the bond index of the UBI-QEP theory or the heat of chemisorption of the species. At this stage, rigorous optimization tools may be employed if deemed necessary.<sup>24</sup> Finally, the modified parameters were assessed against additional experiments (not included in the refinement process).

This refinement methodology bypasses simple optimization of model parameters against experimental data and capitalizes on the interplay between fundamental model development, chemistry-analysis, and experimental data. Given the huge number of parameters of microkinetic models, a purely SA-based optimization can lead to agreement with experimental data without giving a mechanistically correct model and be limited to a narrow range of experimental conditions.

Table 3 reports the parameters of the new mechanism. Since the experimental data considered herein are not affected from reactions 83 to 104 of the original model (methanol and formaldehyde decomposition), we report only the first 82 reactions (the rest remain as published). Heats of chemisorption and a summary of the expressions for the calculation of the activation energies according to the UBI-QEP formalism<sup>28</sup> are given in Tables 4 and 5, respectively. Below, we discuss two examples of the hierarchical data-driven refinement methodology.

### Case studies: Catalytic partial oxidation (CPO) ignition and steam reforming (SR)

Figure 2 compares the experimental data for CPO using the original (left panels), and the revised (right panels) mech-

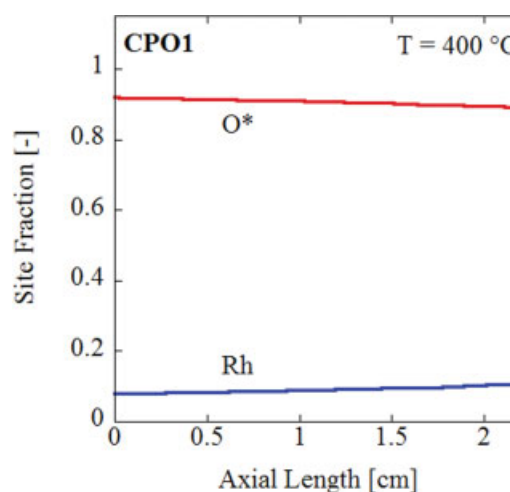


**Figure 3. Partial oxidation: surface coverages of major surface species at 400°C using the original mechanism for partial oxidation (CPO1).**

[Color figure can be viewed in the online issue, which is available at [www.interscience.wiley.com](http://www.interscience.wiley.com).]

anism. In this and subsequent graphs, dash-dotted lines represent the equilibrium composition (obtained using a different code). In the original mechanism, a high Rh specific surface was needed ( $20,000 \text{ cm}^{-1}$ ) in order to observe ignition. Microkinetic analysis at low-temperatures, where the  $\text{O}_2$  conversion is incomplete, indicated that the RDS is the  $\text{CH}_4$  dissociative adsorption



This finding is in agreement with experiments. However, tuning the parameters of reaction  $\text{R}_{55}$  within the uncertainty (the sticking coefficient cannot be higher than 1, and the activation energy of  $\text{CH}_4$  dissociative adsorption is experimentally known to be  $\sim 10 \text{ kcal/mol}$ <sup>35,36</sup>) was insufficient to recover good agreement with the experimental data with the measured Rh specific surface. Analysis of surface coverages points out that the dominant surface species is  $\text{O}^*$ , with a surface coverage higher than 85% (Figure 3). As a result,  $\text{O}-\text{O}$  (adsorbate-adsorbate) interactions could play a significant role in model predictions. This was indeed confirmed via SA in the heat of chemisorption of  $\text{O}$  (not shown). Oxygen adsorbate-adsorbate interactions have been reported.<sup>30,37–39</sup> For example, Wilke et al.<sup>39</sup> proposed a value of  $-21 \text{ kcal/mol}$  ( $Q_{\text{O}^*} = 100 - 21\theta_{\text{O}}$  kcal/mol) on the basis of DFT calculations on Rh(111). In order to get correctly the experimental ignition, we chose an interaction energy of  $-26 \text{ kcal/mol}$  ( $Q_{\text{O}^*} = 100 - 26\theta_{\text{O}}$  kcal/mol; within the uncertainty range of DFT). With this modification, the agreement with the experiments became satisfactory (Figure 2—right panels).

Note that using a large specific surface of Rh (Figure 2—left panels) gives reasonable agreement between data and model predictions. This example underscores the difficulty in using data where the catalyst has not been characterized or data from multiple catalysts (e.g., single crystals and supported catalysts) that may exhibit somewhat different heats of adsorption. At the same time, this example illustrates the effect of uncertainty in a single parameter (in this case in the adsorbate-

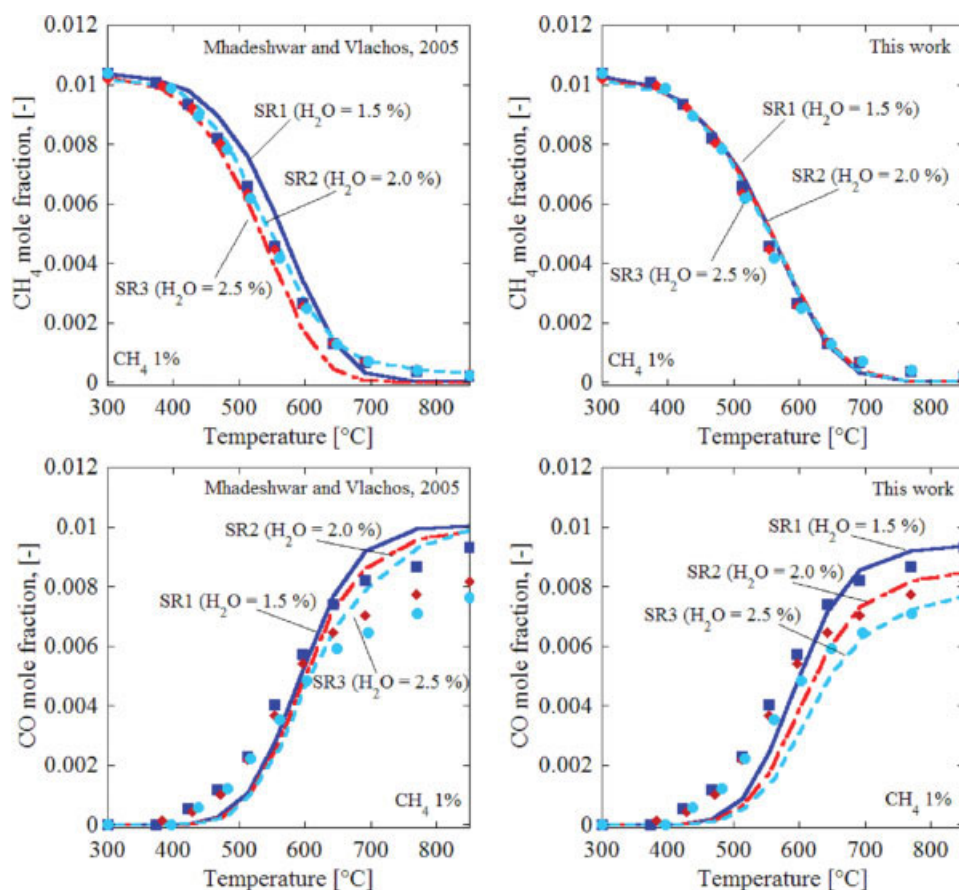


**Figure 4. Steam reforming.**

Comparison between model predictions (lines), and data (symbols) for SR1, SR2, and SR3 using the original and revised mechanism at different isothermal reactor temperatures. [Color figure can be viewed in the online issue, which is available at [www.interscience.wiley.com](http://www.interscience.wiley.com).]

adsorbate interactions) on the estimation of another (e.g., the specific area of Rh). Since surface area multiplies pre-exponential factors, this is an example of the compensation effect.

Figure 4 compares model predictions to experimental data for the  $\text{CH}_4/\text{H}_2\text{O}$  reacting system, both with the original mechanism (left panels), and with the revised one (right panels). In this case, the mechanism of Mhadeshwar and Vlachos provided a reasonable prediction of the  $\text{CH}_4$  mole fraction using the same value of Rh specific surface inferred from the chemisorption experiments, but over predicted the syngas at high-temperatures, and gave an incorrect reaction order with respect to water. In particular, contrary to the experimental evidence,<sup>21,22,40</sup> an increase in methane conversion was predicted with increasing water content in the feed mixture. SA indicated that the RDS of the original mechanism was (Figure 5)



The oxidizer  $\text{OH}^*$  forms from water dissociation ( $\text{H}_2\text{O}^* + * \rightarrow \text{OH}^* + \text{H}^* - R_7$ ). Since the RDS involves a  $\text{H}_2\text{O}$ -related species ( $\text{OH}^*$ ), a dependence of the SR rate on water is predicted. In order for  $R_{79}$  not to be the RDS, it

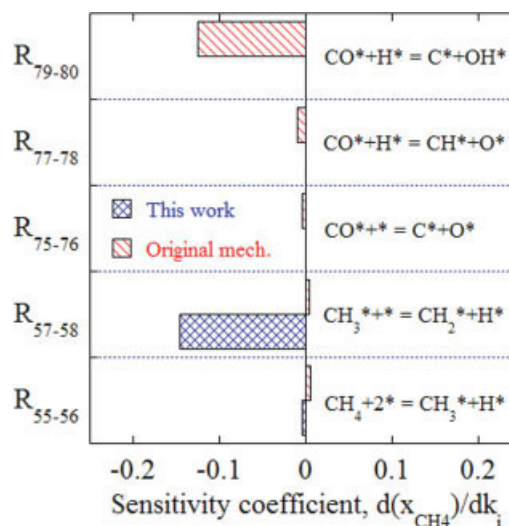


**Figure 5. Sensitivity of methane conversion in steam reforming.**

Use of original and revised mechanism for SR1 test at 500 °C. [Color figure can be viewed in the online issue, which is available at [www.interscience.wiley.com](http://www.interscience.wiley.com).]



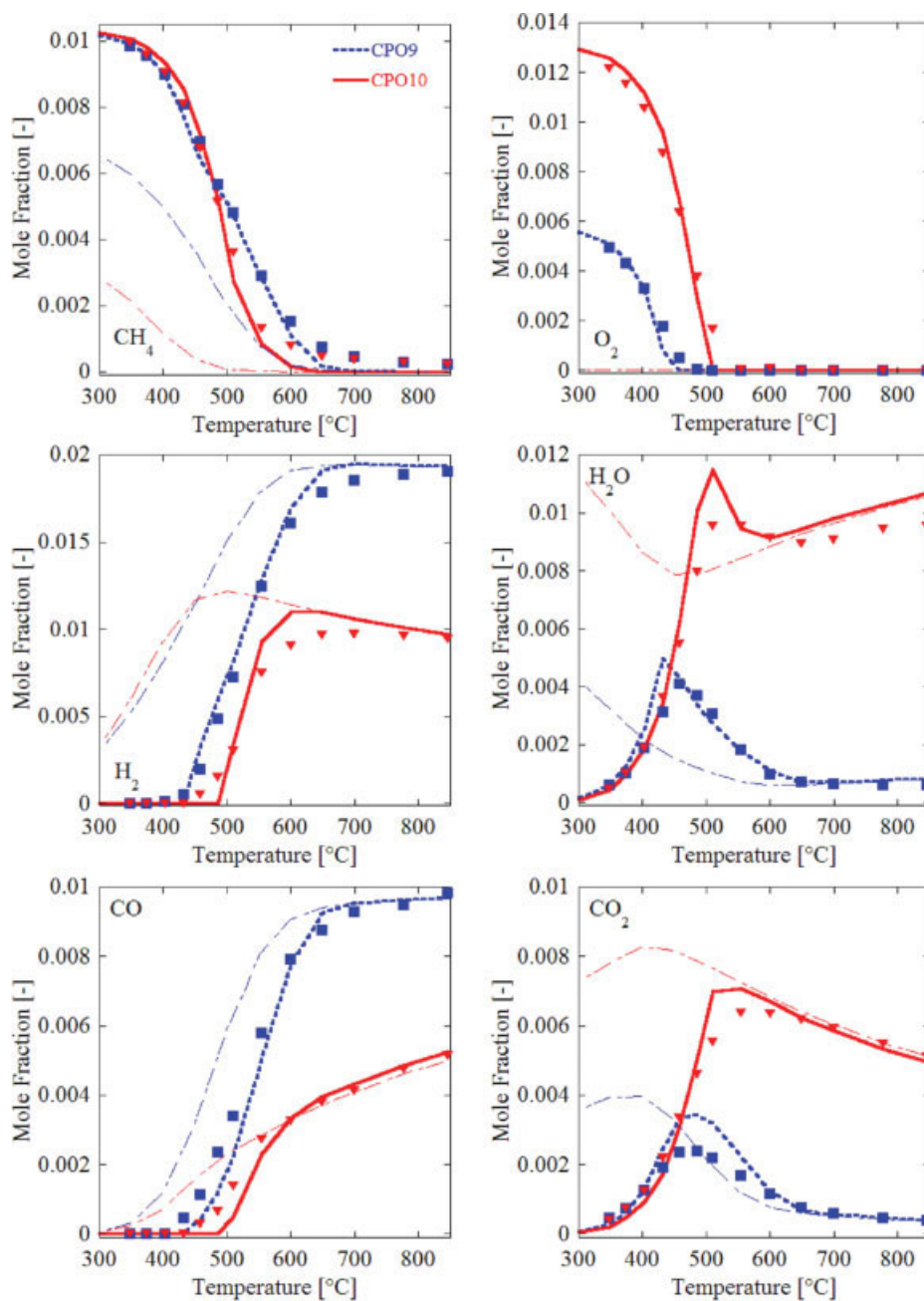


**Figure 6. Partial oxidation.**

Comparison of CPO9 and CPO10 data to model predictions of major species using the revised mechanism (thick lines) at different isothermal reactor temperatures. Rh specific surface from chemisorption experiments ( $600 \text{ cm}^{-1}$ ). Thin dash-dotted lines depict the equilibrium composition obtained using GasEq.<sup>45</sup> [Color figure can be viewed in the online issue, which is available at [www.interscience.wiley.com](http://www.interscience.wiley.com).]

needs to be quasi-equilibrated.<sup>41,42</sup> So, we speeded up  $R_{79-80}$  by changing the bond index from 0.5 (default choice in the UBI-QEP framework<sup>28</sup>) to 0.15, and by increasing the pre-exponential by an order of magnitude. By doing so, the RDS became the CH<sub>4</sub> pyrolysis (specifically  $R_{57}$ , Figure 5), and the reaction rate became independent of the water concentration. With this change, the RDS was qualitatively consistent with experimental findings; fine-tuning of, for example, the pre-exponential of reactions  $R_{57}$  to  $R_{62}$  allowed reasonable quantitative agreement with the experimental data (Figure 4—right panels).

It is worth noting that the comparison between the original model prediction and experimental data, reported in Figure 4 (left panels), could be considered satisfactory, when we consider one experiment at the time. Therefore, one could improve the overall quantitative agreement just on the basis of SA results via changing the parameters of the most sensitive reactions (i.e.,  $R_{79-80}$  according to the original mechanism) to better match the experimental data. However, in doing so, even if the agreement with the experiments were satisfactory, the RDS would be incorrect. The proposed approach is feasible only if a comprehensive, kinetically rele-

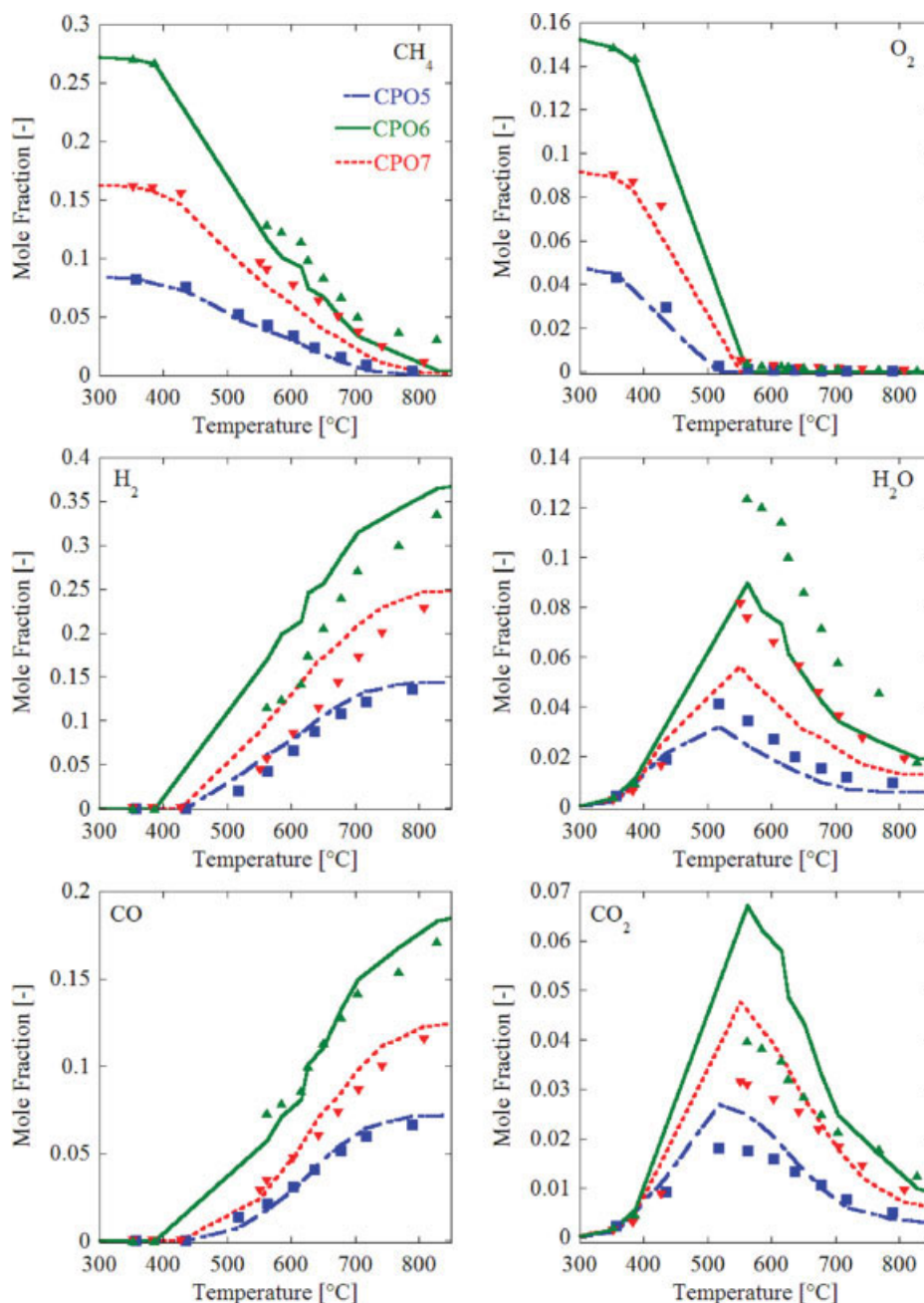


**Figure 7. Partial oxidation.**

Comparison of data (symbols) for CPO5, CPO6 and CPO7 to model predictions (lines) using the revised mechanism for all major species vs. average reactor temperature. Temperature profiles—reported in Figure 8—have been input in these simulations. Rh specific surface from chemisorption experiments ( $600 \text{ cm}^{-1}$ ). [Color figure can be viewed in the online issue, which is available at [www.interscience.wiley.com](http://www.interscience.wiley.com).]

vant data set is available. However, novel approaches to design of experiments may reduce the number of necessary data.<sup>43</sup>

#### Assessment of the reaction model

Additional tests in the annular reactor of Refs. 21, 22 (Table 1) were used for assessment of the microkinetic model. The Rh specific surface has been set as an input from chemisorption experiments. Figure 6 compares data from two CPO

tests at two different  $\text{O}_2/\text{CH}_4$  ratios (namely: 0.56 – CPO9 and 1.30 – CPO10) with model predictions. In both cases, the agreement between model predictions and experiments for reactants and products is good. It is worth noting the good agreement in the  $\text{O}_2$  mole fraction and, in particular, the similar slopes vs. temperature: this level of agreement provides support for the modification of the O adsorbate-adsorbate interactions (see earlier).

Figure 7 compares model predictions and experimental data for different reactant dilutions. Even at high  $\text{CH}_4/\text{air}$

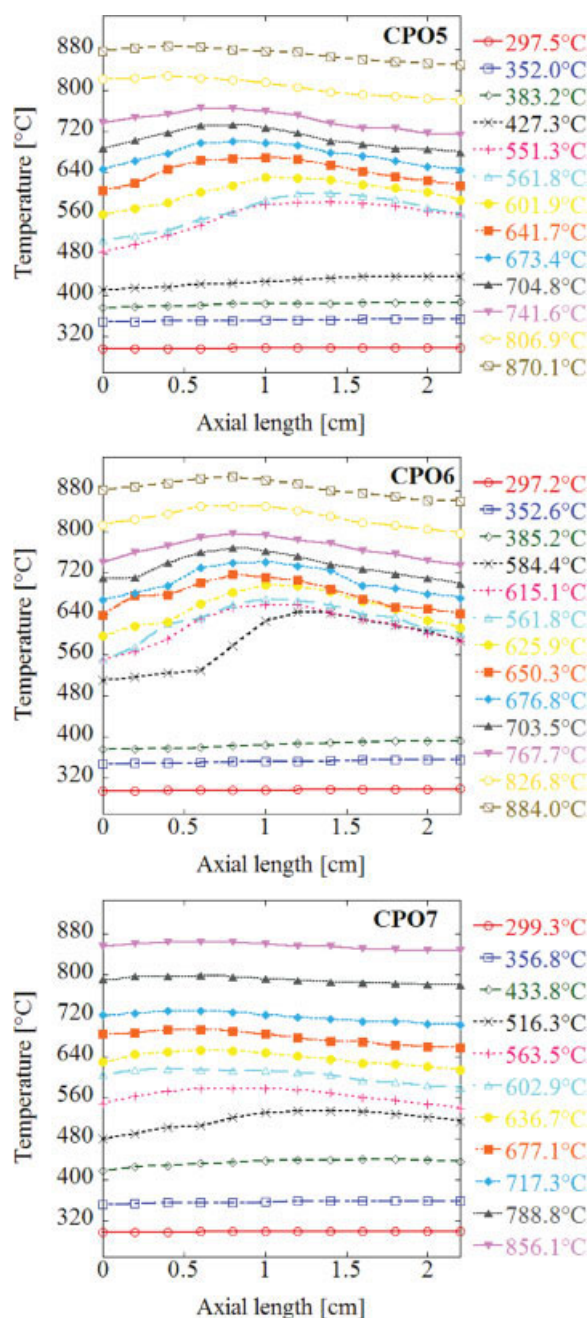


**Figure 8. Partial oxidation.**

Experimental temperature profiles for partial oxidation tests CPO5, CPO6, and CPO7. The legend reports the average profile temperature used in computing the effluent mole fractions in Figure 7. [Color figure can be viewed in the online issue, which is available at [www.interscience.wiley.com](http://www.interscience.wiley.com).]

concentrations, the ignition is correctly predicted ( $O_2$  panel). For temperatures higher than 400 °C, the model tends to slightly overestimate the methane conversion, and, in particular, for CPO6 ( $CH_4$ /air mixture), underestimation of  $H_2O$  and overestimation of  $CO_2$  are observed. However, the maximum difference is of the order of 3% v/v; overall, the agreement is fairly good. In these tests, due to the nondiluted conditions, the experimental axial temperature profile (Figure 8) was inputted in the simulations.

In Figure 9, a CPO test with co-feeding of  $CO_2$  is presented (CPO4). The comparison between model predictions (solid lines) and experiments (symbols) is still good; the model is able to quantitatively account for the  $CO_2$  increase first and its consumption at higher-temperatures.

Overall, it was found that the model is able to predict correctly the behavior of several reacting mixtures, including  $CH_4/H_2O$  and  $CH_4/CO_2$  reforming<sup>44</sup> (an example is shown in

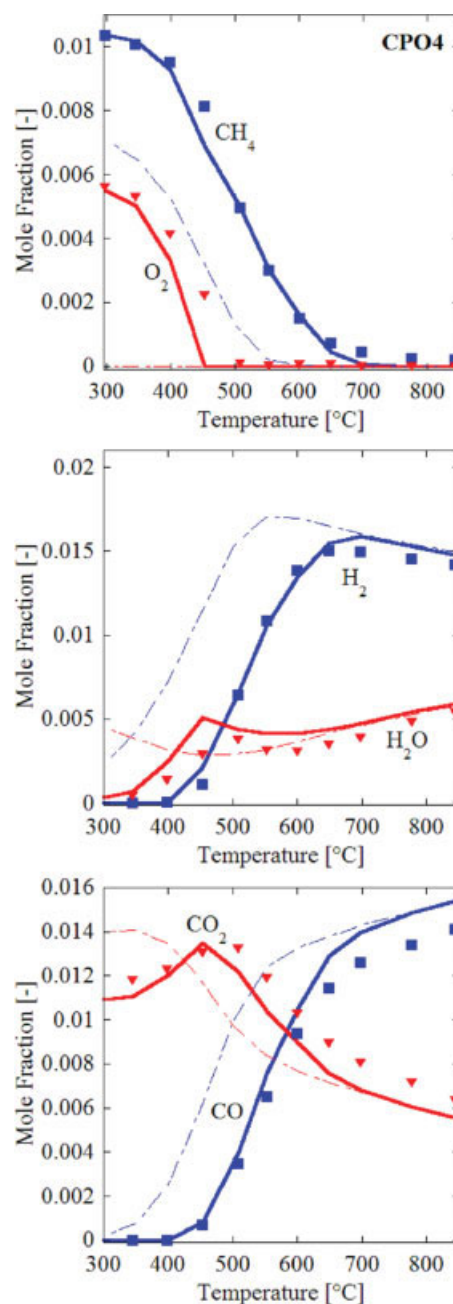


**Figure 9. Effect of  $CO_2$  co-feeding.**

Comparison between new model predictions (solid lines), and experimental data for CPO4 (symbols) at different isothermal reactor temperatures. Rh specific surface from chemisorption experiments ( $600 \text{ cm}^2$ ). Dash-dotted lines depict the equilibrium composition obtained using GasEq.<sup>45</sup> [Color figure can be viewed in the online issue, which is available at [www.interscience.wiley.com](http://www.interscience.wiley.com).]



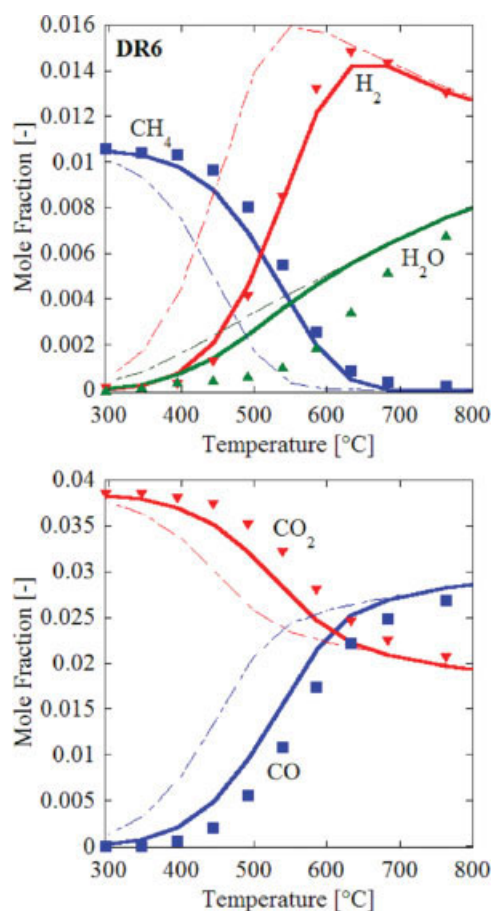


**Figure 10. Dry reforming.**

Comparison between model predictions (solid lines) and experimental data (symbols) for DR6 at different isothermal reactor temperatures. Rh specific surface from chemisorption experiments ( $600 \text{ cm}^{-1}$ ). Dash-dotted lines depict the equilibrium composition obtained using GasEq.<sup>45</sup> [Color figure can be viewed in the online issue, which is available at [www.interscience.wiley.com](http://www.interscience.wiley.com).]

Figure 10), as well as CPO, H<sub>2</sub> and CO rich combustion at different temperatures, compositions and GHSV (here only a select set of data is shown). For WGS and reverse-WGS (Figure 11) reacting systems, the model tends to reach equilibrium faster than the experiments indicate. This represents a weakness of the model and is responsible for the deviation between experiments and model predictions in the CO/CO<sub>2</sub> ratio at intermediate temperatures in CPO tests (e.g., Figure 7). Given the wide range of temperatures and compositions simulated (e.g., Figure 9—CPO with CO<sub>2</sub> co-feeding), and that the mechanism of the WGS and its reverse is still debated (a more systematic analysis on the CO<sub>2</sub> pathways is given in Ref. 44), the overall agreement is reasonable but not great. Extension of microkinetic models to account for support effects in the WGS chemistry may be necessary in future work.

The equilibrium composition (obtained using the GasEq code<sup>45</sup>) depicted with dash-dotted lines in multiple graphs (Figures 2, 6, 9, 10, and 11) indicates that at high-temperatures the system approaches equilibrium, and the model is consistently able to recover this limit. In addition, at low to

moderate temperatures, the reaction system is far from equilibrium, and, thus, useful kinetic information can be obtained for model development and assessment.

### Comparison with other models

Recently, Schmidt and coworkers compared<sup>46</sup> the performance of various microkinetic models<sup>23,47</sup> under a rather limited set of conditions. They concluded that the mechanism of Deutschmann and coworkers behaved better. In this section, we compare three models (this work, and those of Mhadeshwar and Vlachos<sup>23</sup> and Deutschmann and coworkers<sup>47</sup>) in parity plots for all the experiments reported in Table 1. We have considered the Deutschmann model of Ref. 47 (including the coverage dependences of O and CO in their heat of chemisorption).

This comparison is undertaken for a fairly comprehensive set of data and various processes. Figure 12 shows significant improvement of the revised model with respect to the model of Ref. 23. The new model is also more reliable than

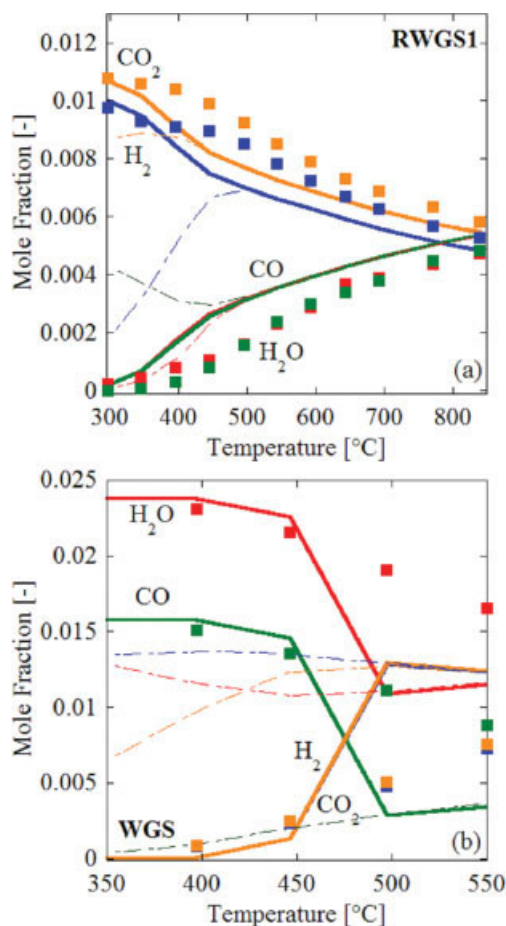


**Figure 11. Water-gas shift and reverse water-gas shift.**

Comparison between model predictions (solid lines) and experimental data for RWGS1 (panel a) and WGS (panel b) at different isothermal reactor temperatures. Rh specific surface from chemisorption experiments ( $600 \text{ cm}^{-1}$ ). Dash-dotted lines depict the equilibrium composition obtained using GasEq.<sup>45</sup> [Color figure can be viewed in the online issue, which is available at [www.interscience.wiley.com](http://www.interscience.wiley.com).]



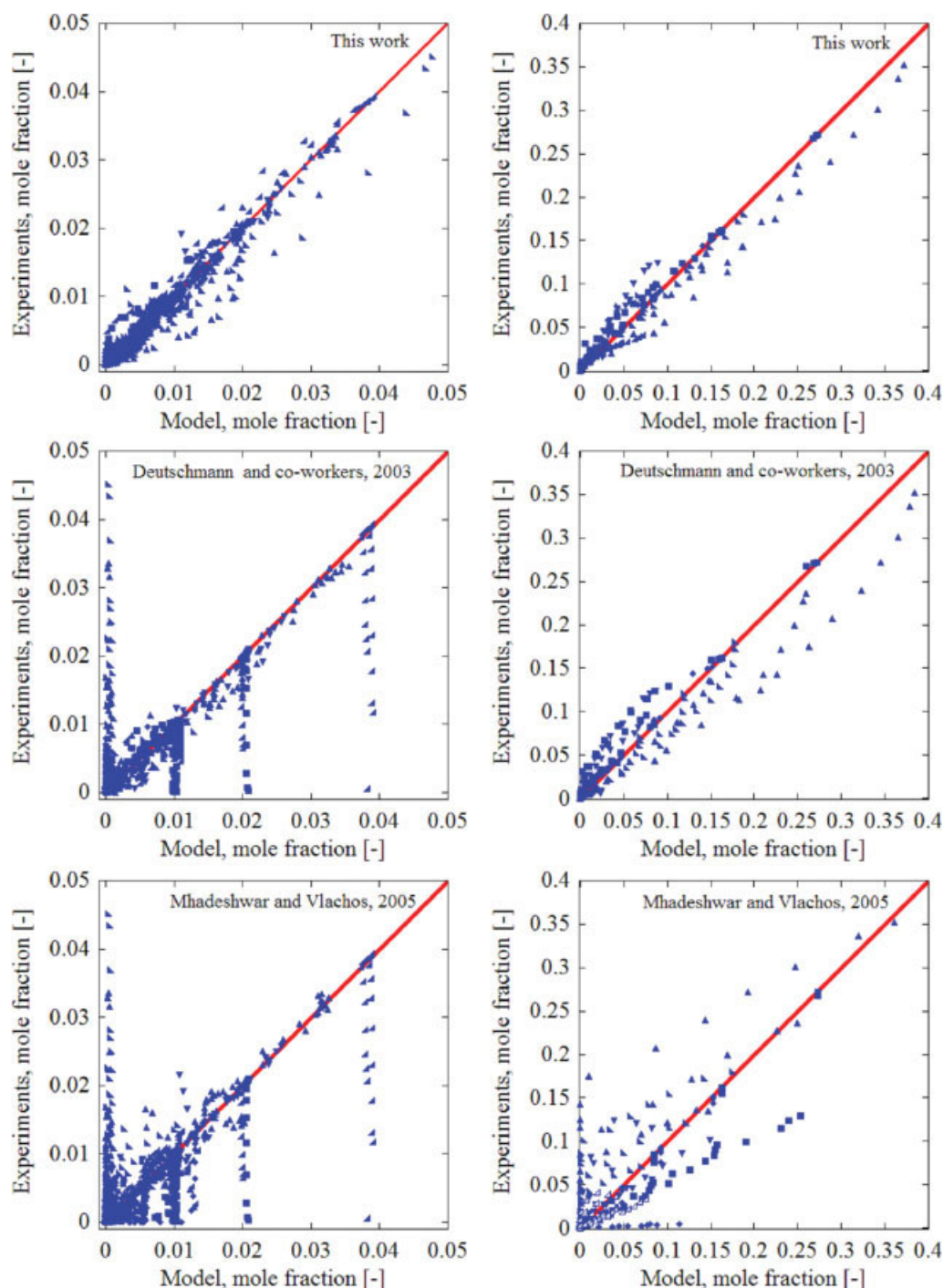


**Figure 12. Parity plots: model prediction vs. experimental data for diluted (left panels), and nondiluted (right panels) mixtures for three mechanisms indicated.**

All the experiments of Table 1 have been included. Rh specific surface from chemisorption experiments ( $600 \text{ cm}^{-1}$ ). [Color figure can be viewed in the online issue, which is available at [www.interscience.wiley.com](http://www.interscience.wiley.com).]

Deutschmann's model. In particular, Deutschmann's scheme predicts reasonably well the CPO tests for an  $\text{O}_2/\text{CH}_4$  ratio equal to 0.56, even for concentrated  $\text{CH}_4$ -air mixtures, except for the ignition temperature of diluted mixtures. At different values of  $\text{O}_2/\text{CH}_4$  ratio, such as 1 or 1.3, noticeable differences between experiments and model predictions are observed, especially in the  $\text{CO}_2/\text{CO}$  distribution, resulting even in vio-

lation of the thermodynamic equilibrium at the highest temperatures. Moreover, in Deutschmann's model,  $\text{CO}_2$  does not activate methane: the  $\text{CO}_2$ - $\text{CH}_4$  and the  $\text{CO}_2$ - $\text{H}_2$  mixtures are inert.<sup>49</sup>

In summary, Figure 12 shows that this model is capable of predicting reasonably well integral data of a spectrum of reacting systems over a wide range of conditions. In addition,

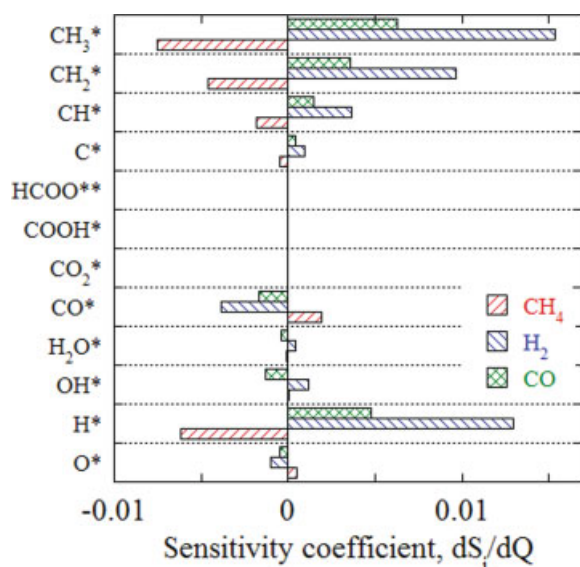


**Figure 13. Sensitivity analysis with respect to species heats of chemisorption in partial oxidation.**

Three responses (mole fractions of  $\text{CH}_4$ ,  $\text{H}_2$ , and  $\text{CO}$ ) are shown for CPO6 at 600 °C. [Color figure can be viewed in the online issue, which is available at [www.interscience.wiley.com](http://www.interscience.wiley.com).]

the model can capture reasonably well spatially resolved data<sup>48</sup> (not shown).

#### Uncertainty analysis due to catalyst variation

In the previous sections, we have shown how intrinsic uncertainty of parameters of microkinetic models can considerably affect model predictions. This uncertainty arises in the estimation of parameters from experimental data, such as when obtaining the heat of chemisorption from temperature programmed desorption (TPD) data, or from theoretical methods, such as UBI-QEP, DFT, and TST.

Aside from the aforementioned uncertainty, a catalyst-related uncertainty exists that arises from the heterogeneity of catalysts samples: the presence of point defects, steps, facets, edges and corners of sites can markedly affect activation energies<sup>31</sup> of certain reactions. In general, the heat of chemisorption of species on supported catalysts may vary with particle size, and for the same particle size, it may vary with particle shape and distribution of sites. For example, in the experimental literature, the CO chemisorption energy (at zero coverage) is reported to be between 30 and 40 kcal/mol.<sup>50</sup> It follows that some of the model parameters can differ with catalyst sample, and, thus, with preparation method, metal precursor chosen, etc., and this variation could be important for structure sensitive reactions.

It would be useful finding out the sensitivity of a model with respect to the heterogeneity of the catalyst. Due to our single-site microkinetic scheme and the mean-field approximation, our model can address this task indirectly. As a reference case, we show this uncertainty analysis for the CPO6 test (Table 1). First, we have performed SA (at high-temperatures, where no  $\text{O}_2$  breakthrough is observed) with respect to the heats of chemisorption. The  $\text{CH}_4$ ,  $\text{CO}$ , and  $\text{H}_2$  outlet

mole fractions were chosen as model responses. Results in Figure 13 show that model predictions are markedly affected from the heat of chemisorption of  $\text{CH}_3$ ,  $\text{CH}_2$  and  $\text{H}$ . Figure 14 shows the effect of uncertainty in the heat of chemisorption of  $\text{CH}_3^*$ , taken to be  $\pm 5$  kcal/mol, i.e.,  $Q_{\text{CH}_3^*} = (42.4 \pm 5)$  kcal/mol, on model prediction. This small ( $\pm 10\%$ ) variation in the heat of chemisorption of  $\text{CH}_3^*$  results in uncertainty of model prediction up to 50%. Similar amplification effects have been found for  $\text{H}$  and  $\text{CH}_2$  (not shown). The

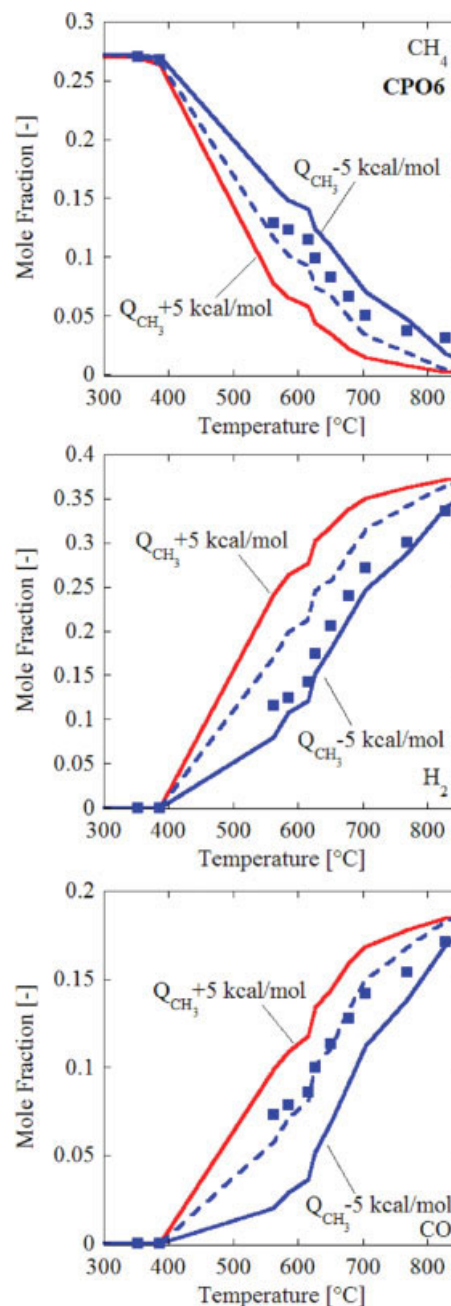


**Figure 14. Uncertainty analysis in partial oxidation.**

Effect of uncertainty in  $\text{CH}_3$  heat of chemisorption on predicted mole fractions of selected species for CPO6. The dashed line represents the simulation with the nominal value. [Color figure can be viewed in the online issue, which is available at [www.interscience.wiley.com](http://www.interscience.wiley.com).]

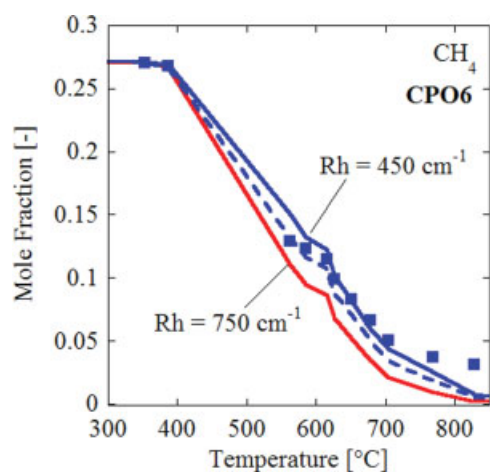


**Figure 15. Uncertainty analysis with respect to Rh dispersion on methane mole fraction for CPO6.**

The dashed line represents the simulation with the nominal value. [Color figure can be viewed in the online issue, which is available at [www.interscience.wiley.com](http://www.interscience.wiley.com).]

high-model sensitivity to the uncertainty in heats of chemisorption for certain species is due to the dependence of activation energies on the heats of chemisorption through the UBI-QEP framework.<sup>28</sup> These simple calculations indicate that substantial differences in activity and selectivity may be expected with catalyst variation for the same surface area for structure sensitive reactions. The structure sensitivity will in turn depend on whether the heats of chemisorption of key intermediates vary significantly with catalyst structure. This is definitely a problem worthy of future work.

Another parameter that is subject to uncertainty is the Rh dispersion. We have varied the specific surface of Rh by  $\pm 25\%$  from its nominal value. Results are shown in Figure 15. The Rh dispersion is just a multiplicative factor of the pre-exponentials, and, consequently, the uncertainty model prediction is proportional to the uncertainty of the parameter.

## Conclusions

In this work we have reported a revised microkinetic model capable of describing multiple processes related to the conversion of natural gas to syngas and hydrogen. The parameters of microkinetic models are subject to intrinsic uncertainty arising from parameter estimation and to the heterogeneity of real catalysts. It was found that this uncertainty could markedly affect model predictions (e.g., even the RDS). In order to make models quantitative and predictive, we have proposed a hierarchical, data-driven methodology, where microkinetic model analysis is used along with a comprehensive, kinetically relevant dataset for incorporation of experimental information in the model parameters. The combination of this methodology with the hierarchical, hybrid methodology outlined in Ref. 23 is essential for the development of a mechanistically sound and quantitative predictive microkinetic model. Overall, the model is thermodynamically consistent, and is able to predict correctly the behavior of several reacting mixtures, including methane steam and dry reforming, catalytic partial oxidation,  $H_2$  and

CO rich combustion, water-gas shift and its reverse over a wide range of temperatures, compositions, reactant dilutions, and space velocities using the experimental Rh dispersion as an input.

In order to assess the effect of the parameter uncertainty arising from catalyst heterogeneity on the overall model prediction, an uncertainty analysis has been performed. This analysis underscored the sensitivity of the model to the heats of chemisorption of some key intermediate species.

While the revised model is a step toward developing more reliable microkinetic models, the deviations seen when comparing the model to some of the data (e.g., with respect to the water-gas shift reaction and its effect in partial oxidation) underscore at the same time its limitations and some of the challenges one needs to consider in future models. Support effects, multiple types of sites, models beyond the mean field approximation, and the dynamics of catalyst nanoparticles with changing reactive environment (e.g., variable surface area for all the experiments reported herein) should be important goals of future experimental and modeling work that could further improve our understanding of surface reaction mechanisms.

## Acknowledgments

MIUR-Rome (PRIN 2006) is gratefully acknowledged for financial support. DGV's work has been supported in part by the NSF (CBET-0651043).

## Notation

$a_v$  = specific surface per unit volume,  $cm^{-1}$   
 $a_{Rh}$  = specific Rh surface per unit volume,  $cm^{-1}$   
 $c_i$  = species concentration,  $mol/cm^3$   
 $d_h$  = hydraulic diameter,  $cm$   
 $D_i$  = species diffusivity,  $cm^2/s$   
 $k_i$  = reaction constant, reaction specific  
 $k_{mat,i}$  = mass-transfer coefficient,  $cm/s$   
 $MW$  = molar mass,  $g/mol$   
 $Q$  = heat of chemisorption,  $kcal/mol$   
 $P_i$  = partial pressure,  $Pa$   
 $r$  = reaction rate,  $mol/cm^2/s$   
 $R_{gas}$  = universal gas constant,  $kcal/mol/K$   
 $Sh$  = Sherwood number  
 $T$  = temperature,  $K$   
 $z$  = reactor axial length,  $cm$   
 $V$  = reactor volume,  $cm^3$   
 $W_i$  = mass flux,  $g/s$

## Greek letters

$\Gamma$  = site density,  $mol/cm^2$   
 $\theta$  = coverage site fraction, dimensionless  
 $\rho$  = gas density,  $g/cm^3$   
 $\omega$  = mass fraction, dimensionless

## Literature Cited

- Ogden JM. Developing an infrastructure for hydrogen vehicles: a Southern California case study. *Int J Hydrogen Energy*. 1999;4:709–730.
- Basile F, Fornasari G, Gazzano M, Kiennemann A, Vaccari A. Preparation and characterisation of a stable Rh catalyst for the partial oxidation of methane. *J Catalysis*. 2003;217:245–252.
- Bauer CG, Forest TW. Effect of hydrogen addition on the performance of methane-fueled vehicles. Part I: effect on SI engine performance. *Int J Hydrogen Energy*. 2001;26:55–70.



4. Bauer CG, Forest TW. Effect of hydrogen addition on the performance of methane-fueled vehicles. Part II: driving cycle simulations. *Int J Hydrogen Energy*. 2001;26:71–90.
5. Kupe J, Zizelman J, Botti, JJ. *Method and system for regeneration NOx adsorbers and/or particulate filters*. 2004: US Patent 6832473.
6. Xu J, Clayton R, Balakotaiah V, Harold MP. Experimental and microkinetic modeling of steady-state NO reduction by H<sub>2</sub> on Pt/BaO/Al<sub>2</sub>O<sub>3</sub> monolith catalysts. *Appl Catal B*. 2008;77:395–408.
7. Moulijn JA, Makkee M, Van Diepen A. *Chemical Process Technology*. New York: Wiley; 2001.
8. NRC. *The hydrogen economy: opportunities, costs, barriers and R&D needs*. Washington, DC: The National Academies Press; 2004.
9. USA, D.o.E.-. *Hydrogen, Fuel Cells and Infrastructure Technologies program*. Available from: [http://www1.eere.energy.gov/hydrogenand-fuelcells/production/natural\\_gas.html](http://www1.eere.energy.gov/hydrogenand-fuelcells/production/natural_gas.html).
10. Norton AG, Deshmukh SR, Wetzel ED, Vlachos DG. Downsizing chemical processes for portable hydrogen production. *Microreact Technol Process Intensification*. 2005;914:179–193.
11. Vlachos DG. Microreaction engineering: processes, detailed design and modeling, in *Microfabricated Power Generation Devices*. Barton PI, Mitsos A, eds. Berlin: Wiley-VCH; 2008. pp. 179–198.
12. Hickman DA, Hauptfear EA, Schmidt LD. Synthesis gas-formation by direct oxidation of methane over Rh monoliths. *Catal Lett*. 1993;17:223–237.
13. Hickman DA, Schmidt LD. Synthesis gas-formation by direct oxidation of methane over Pt monoliths. *J Catal*. 1992;138:267–282.
14. Hickman DA, Schmidt LD. Production of syngas by direct catalytic-oxidation of methane. *Science*. 1993;259:343–346.
15. Tavazzi I, Maestri M, Beretta A, Groppi G, Tronconi E, Forzatti P. Steady-state and transient analysis of a CH<sub>4</sub>-catalytic partial oxidation reformer. *AIChE J*. 2006;52:3234–3245.
16. Choudhary TV, Choudhary VR. Energy-efficient syngas production through catalytic oxy-methane reforming reactions. *Angew Chem Int Ed*. 2008;47:1828–1847.
17. Dumesic JA, Rudd DF, Aparicio LM, Rekoske JE, Trevino AA. *The microkinetics of heterogeneous catalysis*. Washington, DC: American Chemical Society; 1993.
18. Gokhale AA, Kandoi S, Greeley JP, Mavrikakis M, Dumesic JA. Molecular-level descriptions of surface chemistry in kinetic models using density functional theory. *Chem Eng Sci*. 2004;59:4679–4691.
19. Deshmukh SR, Vlachos DG. A reduced mechanism for methane and one-step rate expressions for fuel-lean catalytic combustion of small alkanes on noble metals. *Combust Flame*. 2007;149:366–383.
20. Maestri M, Beretta A, Faravelli T, Groppi G, Tronconi E, Vlachos DG. Two-dimensional detailed modeling of fuel rich H<sub>2</sub> combustion over Rh/Al<sub>2</sub>O<sub>3</sub> catalyst. *Chem Eng Sci*. 2008;63:2657–2669.
21. Donazzi A, Beretta A, Groppi G, Forzatti P. Catalytic partial oxidation of methane over a 4% Rh/ $\alpha$ -Al<sub>2</sub>O<sub>3</sub> catalyst. Part I: kinetic study in annular reactor. *J Catalysis*. 2008;255:241–258.
22. Donazzi A, Beretta A, Groppi G, Forzatti P. Catalytic partial oxidation of methane over a 4% Rh/Al<sub>2</sub>O<sub>3</sub> catalyst. Part II: role of CO<sub>2</sub> reforming. *J Catalysis*. 2008;255:259–268.
23. Mhadeshwar AB, Vlachos DG. Hierarchical multiscale mechanism development for methane partial oxidation and reforming and for thermal decomposition of oxygenates on Rh. *J Phys Chem B*. 2005;109:16819–16835.
24. Aghalayam P, Park YK, Vlachos DG. Construction and optimization of complex surface-reaction mechanisms. *AIChE J*. 2000;46:2017–2029.
25. Mhadeshwar AB, Wang H, Vlachos DG. Thermodynamic consistency in microkinetic development of surface reaction mechanisms. *J Phys Chem B*. 2003;107:12721–12733.
26. Raimondeau S, Vlachos DG. Recent developments on multiscale, hierarchical modeling of chemical reactors. *Chem Eng J*. 2002;90:3–23.
27. Vlachos DG, Mhadeshwar AB, Kaisare NS. Hierarchical multiscale model-based design of experiments, catalysts, and reactors for fuel processing. *Comput Chem Eng*. 2006;30:1712–1724.
28. Shustorovich E, Sellers H. The UBI-QEP method: a practical theoretical approach to understanding chemistry on transition metal surfaces. *Surf Sci Rep*. 1998;31:5–119.
29. Vansanten RA, Neurock M. Concepts in theoretical heterogeneous catalytic reactivity. *Catal Rev Sci Eng*. 1995;37:557–698.
30. Hansen EW, Neurock M. First-principles-based Monte Carlo methodology applied to O/Rh(100). *Surf Sci*. 2000;464:91–107.
31. Liu ZP, Hu P. General rules for predicting where a catalytic reaction should occur on metal surfaces: A density functional theory study of C-H and C-O bond breaking/making on flat, stepped, and kinked metal surfaces. *J Am Chem Soc*. 2003;125:1958–1967.
32. Ibashi W, Groppi G, Forzatti P. Kinetic measurements of CH<sub>4</sub> combustion over a 10% PdO/ZrO<sub>2</sub> catalyst using an annular flow micro-reactor. *Catal Today*. 2003;83:115–129.
33. Tavazzi I, Beretta A, Groppi G, Forzatti P. Development of a molecular kinetic scheme for methane partial oxidation over a Rh/ $\alpha$ -Al<sub>2</sub>O<sub>3</sub> catalyst. *J Catalysis*. 2006;241:1–13.
34. Beretta A, Baiardi P, Prina D, Forzatti P. Analysis of a catalytic annular reactor for very short contact times. *Chem Eng Sci*. 1999;54:765–773.
35. Wang D, Dewaele O, Froment GF. Methane adsorption on Rh/Al<sub>2</sub>O<sub>3</sub>. *J Mol Catal A: Chem*. 1998;136:301–309.
36. Brass SG, Ehrlich G. Internal molecular motions and activated chemisorption: CH<sub>4</sub> on Rhodium. *J Chem Phys*. 1987;87:4285–4293.
37. Hansen E, Neurock M. Predicting lateral surface interactions through density functional theory: application to oxygen on Rh(100). *Surf Sci*. 1999;441:410–424.
38. Stokbro K, Baroni S. The surface chemistry of metal-oxygen interactions: A first-principles study of O:Rh(110). *Surf Sci*. 1997;370:166–178.
39. Wilke S, Natoli V, Cohen MH. Theoretical investigation of water formation on Rh and Pt surfaces. *J Chem Phys*. 2000;112:9986–9995.
40. Wei JM, Iglesia E. Structural requirements and reaction pathways in methane activation and chemical conversion catalyzed by rhodium. *J Catalysis*. 2004;225:116–127.
41. Dumesic, J.A. Analyses of reaction schemes using De Donder relations. *J Catalysis*. 1999;185:496–505.
42. Dumesic JA. Reply to finding the rate-determining step in a mechanism: Comparing DeDonder relations with the “degree of rate control.” *J Catalysis*. 2001;204:525–529.
43. Prasad V, Vlachos DG. Multiscale model and informatics based optimal design of experiments: Application to the catalytic decomposition of ammonia on ruthenium. *Indust Eng Chem Res*. 2008;47:6555–6567.
44. Maestri M, Vlachos DG, Beretta A, Groppi G, Tronconi E. Steam and dry reforming of methane on Rh: Microkinetic analysis and hierarchy of kinetic models. *J Catalysis*. 2008;259:211–222.
45. Morley C. *GasEq: A Chemical Equilibrium Program for Windows*. Available from: <http://www.arcl02.dsl.pipex.com/>.
46. Williams KA, Horn R, Schmidt LD. Performance of mechanisms and reactor models for methane oxidation on Rh. *AIChE J*. 2007;53:2097–2113.
47. Schwiedernoch R, Tischer S, Correa C, Deutschmann O. Experimental and numerical study on the transient behavior of partial oxidation of methane in a catalytic monolith. *Chem Eng Sci*. 2003;58:633–642.
48. Horn R, Williams KA, Degenstein NJ, Schmidt LD. Syngas by catalytic partial oxidation of methane on rhodium: Mechanistic conclusions from spatially resolved measurements and numerical simulations. *J Catalysis*. 2006;242:92–102.
49. Maestri M. *Short-contact-time Catalytic Partial Oxidation of methane on Rh: reactor analysis and microkinetic modeling*. Italy: Politecnico di Milano; 2008. PhD. Thesis.
50. Wei DH, Skelton DC, Kevan SD. Desorption and molecular interactions on surfaces: CO/Rh(110), CO/Rh(100) and CO/Rh(111). *Surf Sci*. 1997;381:49–64.

Manuscript received July 26, 2008, and revision received Nov. 4, 2008.